

Chapter 1

Light-sheet microscopy combined with remote force measurements

Show me a fish

— Anonymous

How multicellular organisms enact the morphogenetic programmes that ensure their characteristic forms remains an enigma. Genetic screens have yielded an array of essential structural, patterning and signalling pathways with which morphogenesis is orchestrated, [1] however, morphogenesis is ultimately a physical phenomenon that requires a physical explanation. *In vivo* imaging of morphogenesis allows measurements to be made that reveal stereotypical patterns in the cellular behaviour of individual, and groups of, cells. These are indicative of active force generation, but are insufficient to construct a quantitative explanation of where forces are generated and how forces propagate within and between tissues. To overcome these limitations, we require a quantitative characterisation of the physical properties of the tissues involved in order to understand how forces propagate within tissues to bring about morphogenesis. Measurements of the properties of individual cells, [1] and of bulk tissues, [2] have revealed properties typical of both viscoelastic and visco-elasto-plastic solids [3]. Bulk tissue properties can be estimated using atomic force microscopy to investigate a tissue surface [18]. Alternatively, micropipette aspiration can probe dissociated cells or explants, however, this method cannot assess deep tissue directly [ref]. More recently, techniques have been developed to measure tissue stress and viscoelastic properties, utilising laser ablation [ref], oil droplets [ref], or embedding tissue explants in matrix gel [ref]. Most recently, ferrofluid

droplets have shown that local tissue properties[in terms of rheological parameters of elasticity and viscosity? Elaborate on these changes.] change with respect to the tissue localisation. [ref] There is still a need for methods that can provide a repeated, real-time readout of physical properties and relate those measurements to the underlying morphogenetic behaviour.

A method was developed that can give non-destructive, quantitative measurements of local tissue physical properties at the length scale of a few cells, completed within seconds to minutes, and repeatable over developmentally-significant periods. To achieve this, biologically-compatible superparamagnetic beads were implanted into developing zebrafish embryos and built a four-pole electromagnetic device that produces a controlled magnetic field gradient in 3D, such that a bead can be moved with known force. Tracking the bead movement gives the dynamic material properties of the surrounding tissue [in terms of elasticity and viscosity? Elaborate on what the system allows you to evaluate.]. This technique was used to study the emergence of the first cohesive tissue of the zebrafish blastula, between the “high” to “sphere” stages of development.

It was found that mesenchymal blastomeres become first motile, and then adherent, to form the tissue that will go on to contribute to the first morphogenetic movement of the embryo. Moreover, there was a three-fold increase in both tissue elasticity and viscosity was associated with the mid-blastula transition. This was dependent upon E-cadherin-based intercellular adhesions and Rac-1-dependent cell protrusion; abrogating either of these processes interfered with the developmental changes of the embryo. Interestingly, reducing Rho-kinase-dependent cell contractility increased both tissue viscosity and elasticity and increased the number of cell protrusions.

By using light-sheet microscopy, in conjunction with magnetic tweezers, the fast image of tissue were acquires on a scale large enough to track the topological changes and rearrangement of cells. The magnitude of change in both of these attributes reduces as tissue elasticity and viscosity increase, and it is evident that the viscoelastic component correlates predominantly to changes in cell morphology, while viscosity dictates the rearrangement of cells.

1.1 Tissue dynamics in developing organisms

1.1.1 Danio rerio as a developmental model organism

The zebrafish (*Danio rerio*) is a key model organism for vertebrate development. It shares features of its body plan and developmental stages (Fig. 1.1) with *Xenopus*, chickens, and mice [2], indicating the existence of conserved developmental mechanisms. These mechanisms rely on reproducible, organism-wide patterns of cellular division, migration, death and differentiation during embryonic developmental stages, as well as during adult life. As this cellular behaviour arises within the context of organism-wide signalling events, a complete understanding of the processes shaping these events requires whole-organism imaging. Of the vertebrate model organisms, the zebrafish is best suited for whole organism imaging from fertilisation until hatching/birth. The embryo is transparent and small, but can still be physically manipulated, and develops externally from the mother, allowing for imaging uninhibited by surrounding tissue from the parent organism; as a result, zebrafish require no atmospheric control to enable growth, unlike cell cultures and other higher order models such as mice. Moreover, zebrafish growth is rapid; a single cell, with a 0.7 mm diameter, becomes a 3.5 mm long larva within three days (see Table 1.1). Zebrafish are also suitable for genetic studies as the genome is fully sequenced and tools for genetic manipulation are readily available. Breeding the fish is simple, as sexual maturity occurs at three months after fertilisation, facilitating easy cross-breeding [?]. Finally, the costs of keeping zebrafish are lower than that of other vertebrates due to their low space requirements and minimal handler time [3].

1.2 Methods of measuring tissue dynamics

The force generation requirements for the investigation of cellular morphogenesis greatly limits which techniques would be suitable for force application and its measurement, as the forces must be applied in the 10 μm to 100 μm length scale, of a similar length to the size of a cell. Furthermore, the magnitude of these forces should be in the 10 μN to 100 μN range, of a similar magnitude to the forces that cells are able to generate []. It is also desirable for the process to result in minimal heat and light exposure to the organism, as well as to be minimally invasive. Immediately, common techniques such as mechanical probing, atomic force microscopy, and

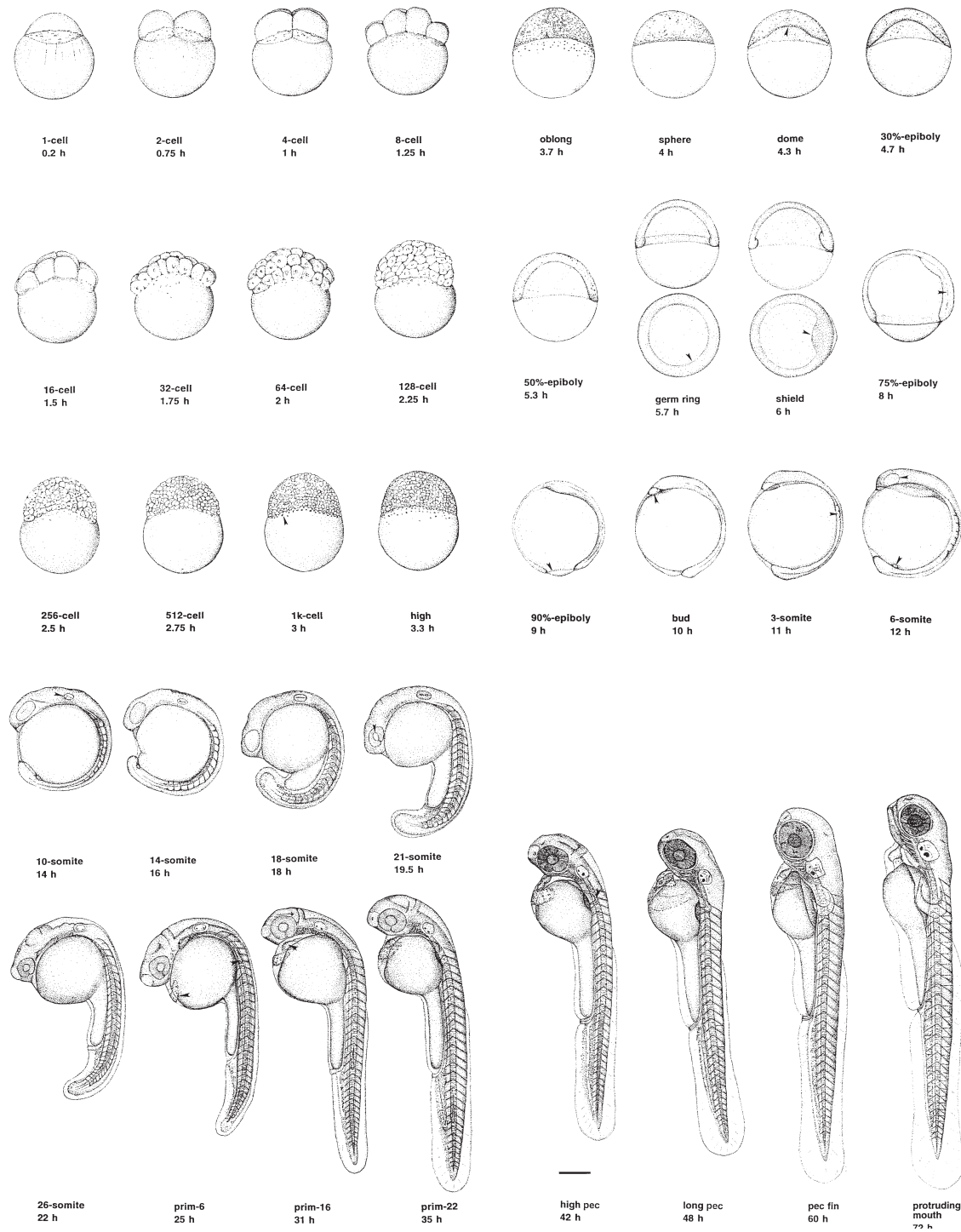


Fig. 1.1 Periods of embryonal development of the zebrafish. The embryo develops from a single cell into a larva in three days, undergoing extensive morphological changes. See Table 1.1.

Age / h	Stage	Notes
0 h	Zygote	Cytoplasm flows to the animal pole to form the blastodisc.
0.75 h	Cleavage	The blastodisc undergoes several rounds of rapid, synchronous, partial cleavage to give 64 blastomeres (and a yolk cell).
2.25 h	Blastula	The mid-blastula transition occurs; epiboly begins.
5.25 h	Gastrula	More cell migration. Gastrulation, involution, convergence, extension; forming formation of the epiblast and hypoblast.
10 h	Segmentation	The tail appears; somites develop; organogenesis starts.
24 h	Pharyngula	Circulation begins and pigmentation develops. The body axis straightens. Fins begin development.
48 h	Hatching	Primary organ systems complete morphogenesis, cartilage develops, the fish hatches.
72 h	Early larva	The swim bladder inflates; food-seeking behaviour occurs.

Table 1.1 Developmental stages of zebrafish

optical tweezers prove intractable. Thus, magnetic tweezers were employed in this work as a method of force application and measurement.

Magnetic tweezers operate under the principle of applying a force to a magnetic bead through a magnetic field gradient and are able to apply this force at a distance, without perturbing biological materials, making the technique minimally invasive. Single-pole tweezer systems, where a single electromagnetic solenoid is able to apply a variable force on a bead in one direction, have been used in a number of experiments to understand the dynamics of cellular force responses []. However, to characterise the force generation in cellular rearrangement fully, it is necessary to generate a magnetic force in an arbitrary direction in three dimensions, as this work demonstrates.

1.2.1 Magnetic tweezers

The design of the magnetic tweezers was based on a previously published design [(Vicci 2003)], which is compatible with large samples, such as the zebrafish embryo employed in this work; and was shown to generate sufficient forces using COMSOL simulations. This section presents the development of the magnetic tweezers

including the imaging chamber required by the Light-sheet Fluorescence Microscopy (LSFM). The mechanical design of the magnetic tweezers was based on a monopole model. In this simplification the magnetic field is assumed to be generated by point sources (monopoles) around a sample containing a magnetic bead. The sum of the aggregated monopole strengths must equal zero because, in nature, there are no actual sources or sinks of magnetic flux (i.e. solenoids generate dipole magnetisation). In this model, a force acting on the bead in the direction of a monopole can be approximated by [?]. The magnetic dipole moment, \mathbf{m} , induced in the bead by a magnetic field, B , is given by:

$$\mathbf{m} = \frac{\pi d^3}{2\mu_0} \frac{\mu_r - 1}{\mu_r + 2} \mathbf{B} \quad (1.1)$$

A force, proportional to the magnetic dipole moment, is then exerted on the bead in the presence of magnetic field gradients:

$$\mathbf{F} = \frac{\pi d^3}{2\mu_0} \frac{\mu_r - 1}{\mu_r + 2} \nabla \mathbf{B}^2 \quad (1.2)$$

where d is the diameter of the bead, μ_0 is the magnetic permeability of free space, μ_r is the relative magnetic permeability of the bead and \mathbf{B} is the magnitude of the field generated by a magnetic monopole. \mathbf{B} is in the form of $\frac{B_p}{r^2}$ where B_p is the monopole strength and r is the distance from the monopole. Hence the gradient $\nabla \mathbf{B}$ of the field is $2\frac{B_p}{r^3}$, and the force on the bead proportional to $2\frac{B_p^2}{r^5}$ [(Vicci 2003)]. In the mechanical design of the magnetic tweezers, it was thus desirable to position magnetic poles as close as possible to a sample.

A minimum of four monopoles is required to achieve effective 3D specification of the force acting on the bead. The optimal configuration is a tetrahedral geometry, where monopoles are distributed on the vertices of a tetrahedron. Deviation from this geometry limits the range and directionality of achievable forces. Finally, only a single bead should be used at a time, as agglomeration of beads influences the magnetic field distribution due to the interactions between the beads, and thus disturbs the monopole model [M\IeC\{"o\}ller et al. 2003]. The magnitudes and gradients of the magnetic

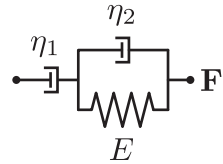


Fig. 1.2 Viscoelastic model for embryonic tissue used in this work; consisting of a dash-pot in series with a dash-pot and spring in parallel. The spring, E , represents the stiffness of the ensemble tissue, the first dash-pot (η_1) represents tissue viscosity and the second dash-pot (η_2) represents cellular viscosity.

field in the space between the poles is controlled by four solenoid coils; by varying the currents in these coils independently, one may control the the magnitude and direction and magnitude of the force acting on the bead.

Model Theory

The simplest phenomenological model capable of mimicking the viscoelastic response of a developmentally early zebrafish embryo, subject to strain generated by a moving, spherical, rigid object, is a one-dimensional linear combination of an elastic spring and viscous dash-pots. More precisely, the model assumes a parallel spring and dash-pot [(Kelvin\IeC {-}Voigt model)] in series with a second dash-pot, see Fig. 1.2.

The model is described by the following parameters: dynamic viscosities, η_1 and η_2 , and elastic stiffness, E . When a strain σ is applied, the spherical rigid object, in this case a magnetic bead made of superparamagnetic nanoparticles embedded into a polyester matrix, moves and the displacement is quantified by the strain ϵ . The same parameter is used to evaluate the recovery phase, when $\epsilon = 0$. The experimental protocol used here consists of two phases: the creep phase, where from equilibrium the state at $t = 0$ an instaenous and constant force is applied on the bead and kept for a given time t_1 (60 s); and the recovery phase where the force is removed at t_1 and the bead displacement is monitored for a suitable time period (120 s). To model the equations of motion the a linear spring is described by:

$$\epsilon = \frac{1}{E}\sigma \quad (1.3)$$

while a dash-pot obeys:

$$\dot{\epsilon} = \frac{1}{\eta} \sigma \quad (1.4)$$

The equation for a spring and a dash-pot connected in parallel follows as:

$$\sigma = \sigma_E + \sigma_{\eta_2} = E\epsilon_p + \eta_2 \dot{\epsilon}_p \quad (1.5)$$

$$\ln \left(\frac{\sigma}{\eta_2} - \frac{E}{\eta_2} \epsilon_p \right) = -\frac{E}{\eta_2} t + \ln C_1 \quad (1.6)$$

Setting the initial conditions of $\epsilon_p = 0$ at $t = 0$:

$$\epsilon_p = \frac{\sigma}{E} \left(1 - \exp \left(-\frac{E}{\eta_2} t \right) \right) \quad (1.7)$$

The temporal variation of the dash-pot is ruled by:

$$\sigma = \eta_1 \dot{\epsilon}_s \implies \epsilon_s = \frac{\sigma}{\eta_1} t \quad (1.8)$$

Knowing that $\epsilon = \epsilon_s + \epsilon_p$, the strain variance is therefore:

$$\epsilon = \frac{\sigma}{\eta_1} t + \frac{\sigma}{E} \left(1 - \exp \left(-\frac{E}{\eta_2} t \right) \right) \quad (1.9)$$

During the second phase, which starts at t_1 , the force is no longer applied and the total strain is given by the previous displacement of η_1 dash-pot blocked at $t = t_1$, and the relaxation of the Kelvin-Voigt model which is described by:

$$E\epsilon_p + \eta_2 \dot{\epsilon}_p = 0 \implies \epsilon_p = C_2 \exp \left(-\frac{E}{\eta_2} t \right) \quad (1.10)$$

From the continuity of strain and $t = t_1$, C_2 becomes:

$$\frac{\sigma}{\eta_1}t + \frac{\sigma}{E} \left(1 - \exp\left(-\frac{E}{\eta_2}t_1\right)\right) = C_2 \exp\left(-\frac{E}{\eta_2}t\right) \quad (1.11)$$

$$C_2 = \frac{\sigma}{E} \left(\exp\left(\frac{E}{\eta_2}t_1\right) - 1\right) \quad (1.12)$$

So, for $t \geq t_1$, the strain is:

$$\epsilon = \frac{\sigma}{\eta_1}t_1 + \frac{\sigma}{E} \left(\exp\left(\frac{E}{\eta_2}t_1\right) - 1\right) \exp\left(-\frac{E}{\eta_2}t\right) \quad (1.13)$$

The equations of motion may be summarised as

$$\epsilon = \begin{cases} \frac{\sigma}{\eta_1}t + \frac{\sigma}{E} \left(1 - \exp\left(-\frac{t}{\tau_2}\right)\right) & \text{for } t \geq t_1 \\ \frac{\sigma}{\eta_1}t_1 + \frac{\sigma}{E} \left(\exp\left(\frac{t_1}{\tau_2}\right) - 1\right) \exp\left(-\frac{t}{\tau_2}\right) & \text{for } t \leq t_1 \end{cases} \quad (1.14)$$

where $\tau_2 = \frac{\eta_2}{E}$

A bead moving through a viscous fluid can be described by Stokes' law $F = 6\pi\eta'r\nu$, where r is the radius of the bead and ν is the critical velocity of the bead. Stokes' law may be written as:

$$F = 6\pi\eta'r \frac{dx}{dt} \quad (1.15)$$

$$\Rightarrow \frac{F}{\pi r^2} = 6\eta' \frac{d}{dt} \frac{x}{r} \quad (1.16)$$

$$\Rightarrow \sigma = 6\eta' \frac{\epsilon}{dt} \quad (1.17)$$

Giving the equation of a dash-pot

$$\dot{\epsilon} = \frac{\sigma}{\eta} \quad (1.18)$$

To model the elastic spring, the elastic response of the tissue due to the bead displacement is approximated by the Thomson's solution of a point force in an infinite isotropic medium [4]. The displacement (\mathbf{u}) in cylindrical coordinates ((p, z)) for a point force (F_z) located at the origin and directed along (z) axis is given by:

$$\mathbf{u} = \frac{F_z}{4\pi\mu r} \left[\frac{pz}{4(1-v)r^2} \hat{\mathbf{p}} + \left(1 - \frac{p^2}{4(1-v)r^2}\right) \hat{\mathbf{z}} \right] \quad (1.19)$$

Where $\hat{\mathbf{p}}$ and $\hat{\mathbf{z}}$ are unit vectors, μ is the shear modulus (deformation at constant volume) and v is Poisson's ratio (a negative ratio of transverse to axial strain of a specimen, under an axial force). As only forces in the $\hat{\mathbf{z}}$ direction are being considering, Equation (1.19) becomes:

$$u_z = \frac{F_z}{4\pi\mu r} \left[\left(1 - \frac{p^2}{4(1-v)r^2}\right) \right] \quad (1.20)$$

Evaluating the displacement only on the z axis where $p = 0$, reduces this to:

$$\nabla z = \frac{F_z}{4\pi\mu r} \quad (1.21)$$

In the close proximity to the bead of radius r_{bead} , the displacement is given by:

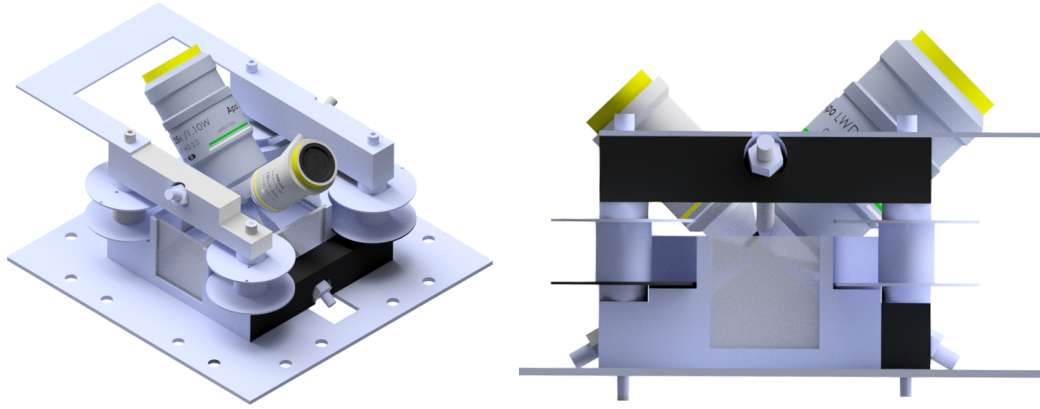
$$\frac{\nabla z}{r_{\text{bead}}} = \frac{1}{4\mu} \frac{F_z}{\pi r_{\text{bead}}^2} \implies \epsilon = \frac{1}{4\mu} \sigma \quad (1.22)$$

Which is equivalent to (1.3) when substituting E with 4μ .

$$(1.23)$$

1.2.2 Magnetic tweezer design

In the magnetic tweezer systems a square loop of iron was used to carry magnetic flux from four solenoids to four embedded magnetic tips. The lower magnetic tips were mounted azimuthally at 30° , allowing for the very large 1.1 NA, long working distance, Nikon, objective lens to image the magnetic centre of the magnetic poles. However, this allowance for the large objective lens by re-orientating the tweezer



(a) Light-sheet objective lens placed within the magnetic tweezer chamber. **(b)** Side view with magnetic centre of tweezers at the double focus of the illumination and imaging objective lenses.

Fig. 1.3 CAD designs of the magnetic tweezer housing coupled to the light-sheet objectives.

poles reduces the maximum magnetic field strength by 10 %. Orienting the poles at the optimal angle to the azimuth (45°) would provide 2.33 T from COMSOL simulations.

Imaging Chamber Design

The imaging chamber presented in Fig. 1.4 was 3D printed with Acrylonitrile Butadiene Styrene (ABS) to allow for modular and rapid re-design. Clear acrylic windows were added to allow for a positioning camera (PiCam) to be placed below the tweezer system, as seen in Fig. 1.3 (b), which aided with the positioning of the zebrafish. The chamber was watertight and featured heating pads to maintain the embryo medium and zebrafish at 28.5 °C during imaging.

Force calibration

The 3D magnetic field gradient generated by the quadrupole was shaped by a combination of currents to obtain forces in the range of 8 nN. Force calibration was realised by analysing the velocities of a $41.17 \mu\text{m}$ diameter paramagnetic bead in silicone oil of known viscosity at different combinations of intensities of currents. The coordinate systems of the magnetic tweezers and the light-sheet system had to be aligned due to the non-linear decline of force of the magnetic field away from the magnetic centre. This was achieved by defining an origin within the tweezer system itself, where force in every direction was maximal. This point was then

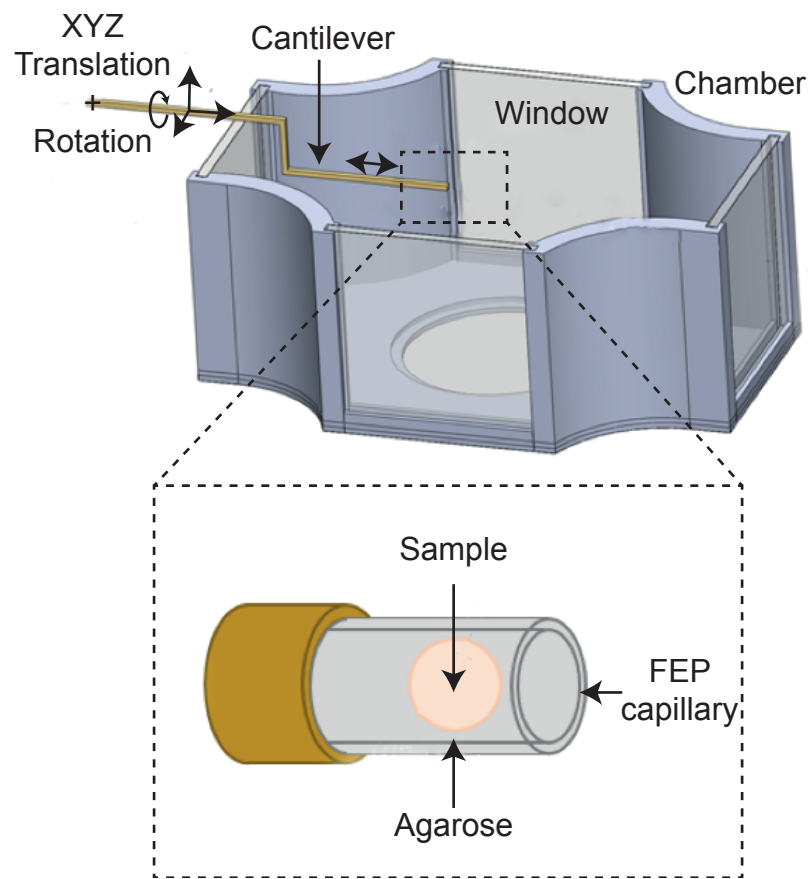


Fig. 1.4 3D printed chamber for housing the magnetic tweezers whilst providing ambient living conditions for a developing zebrafish.

recorded by inserting a fiducial magnetic bead, which was attached to an arm and positioned using micrometer screws. Once the tweezer system was fixed to the light-sheet system, the automated stage was driven such that the fiducial bead was at the imaging centre of the camera and at the axial centre of the piezo objective actuator. The tweezer positioning was coarse-positioned by eye using the automated stage, followed by fine correction utilising the bright-field imaging built into the sample chamber.

Synchronisation

The magnetic tweezers were calibrated and automated using current amplifiers driven by voltages from a Raspberry Pi. Simple Recommended Standard 232 (RS232) commands controlled the amount of force, the direction and the on/off state of the tweezers. These commands were then sent from the LabVIEW controller of the light-sheet system to ensure good synchronisation between the initial drive of the bead and the start of the volume acquisition.

1.2.3 Biological methodology

Zebrafish embryos were harvested immediately after fertilisation and incubated at 28.5 °C. Embryo lines that were used were: wild-type (WT), Tg(beta-actin:mCherry-CAAX) (labelling membranes), Tg(beta-actin:Lifeact-eGFP) (labelling F-actin) and Tg(beta-actin:Myosin2- mCherry) (labelling myosin). Transplantations were performed at 1k-cell stage using a tip broken elongated capillary [] mounted on an oil-filled pressurised system controlled by a syringe []. Beads, or cells, were transplanted at 1k-cell stage. Beads were incubated in 4 % BSA for 10 min at 28.5 °C before injecting to reduce the chances of bead rejection from the embryo.

The soft egg sack was removed from around the zebrafish embryo (the chorion) which, if left on, would degrade the optical imaging. A stereo-microscope was used so dechorionation could be done by eye with careful and precise use of very sharp tweezers. This was done in warm embryo medium on a bed of 1 % agarose because exposed embryos will rupture on contact glass. The dechorionated embryos were pipetted into warm low melting point agarose and then immediately drawn up into a length of Fluorinated Ethylene Propylene (FEP) tubing.

Analysis

All tests were performed with R software. A linear mixed effect model was performed to compare rheological parameter trends in different loss-of-function assays. Anova tests compared linear fits on developmental trends of the rheological parameters between Wild type (WT) and loss-of-function conditions (mutants). The percentage bend correlation method was used for correlation between cell and rheological parameters to take outliers into account [5].

1.3 Algorithmic bead tracking

To perform a model fitting, as derived in Equation (1.14), the magnetic bead was tracked algorithmically. Each volume was 2048 voxels \times 2048 voxels \times 100 voxelss, with each volume acquisition taking 5 s. Each push-pull experiment produced 42 volumetric spatial coordinates in time (x, y, z, t), hence the entire data set to be analysed was 172 GB. Two methods of bead tracking were explored, slice-wise Hough transform analysis and template matching.

1.3.1 Hough-based bead tracking

The Hough transform is a feature-tracking mechanism used to transform an image into a space whereby intensity minima or maxima represent circles. These localised maxima correspond to multiple circles in the image space of a given range of radii as provided to the function. In the analysis employed here, the first iteration of the analysis algorithm exhaustively searched for circles, with varying threshold sensitivity, until a single circle (of the correct radius through the image volume) was found. Once singular circles were found slice-wise, a circle was fit to the radii found in each slice to localise the sphere in z . This lead to multiple computationally expensive transforms being applied and the algorithm being slow. It is possible to use a 3D Hough transform that searches for spheres rather than circles; again, multiple matches are likely to be returned, resulting in tracking errors.

1.3.2 Template matching

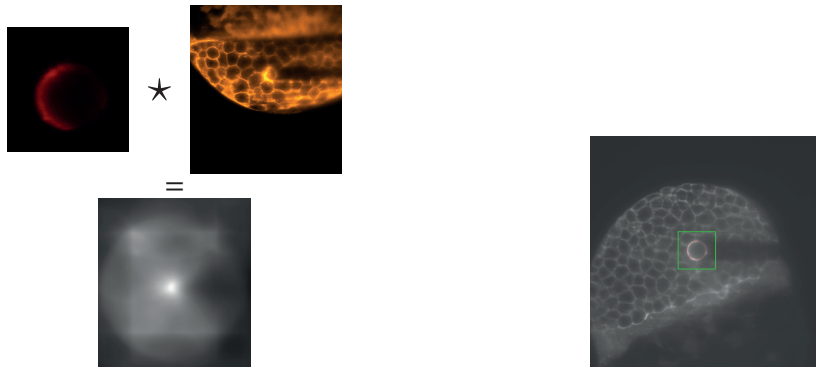
As only a single sphere could be found in each image volume, a template-matching approach was explored. Initially, an ideal bead was extracted from an image volume

for future analyses (see Fig. 1.5a). However, it was found empirically that the ideal bead volume template was more likely to chase cells than an artificially, computed, idealised bead. To construct a virtual bead, a virtual volume was constructed and a white, hollow sphere of the correct pixel radius (160 px) was superimposed.

Template matching techniques fundamentally rely on the cross-correlation of two images or volumes. Cross-correlation is made programmatically quicker by operating in Fourier space for convolution rather than iteratively in image space. Although this does decrease the overall computation time, the net memory usage of the algorithm increases. As such, care has to be taken to avoid Random Access Memory (RAM) overfilling, as this can cause the algorithm to crash; particularly in operating systems without a well-managed swap-space; or cause the swap-space to be used, slowing the algorithm as it reads large Fourier space volumes off of a slower hard-drive.

To circumvent large amounts of memory being used, a windowing technique was employed to ensure that the minimal amount of voxels was needed for analysis. The cuboidal window was set to be twice the pixel radius of the bead in each dimension which was arbitrarily set with the assumption that the bead would not move out of the window between two concurrent time points. Between each frame, the centre of the window was shifted to be aligned with the centre of the bead. The voxels within this window were analysed and the window shifted again by the relevant offset. The bead centres were then exported, in 3D, to a text file for further analysis.

The seed location, in the first frame for the bead, was found in one of two ways. A best guess of bead location was found by downsampling the resolution of the image stack and performing a template match on the stack, after which a finer search was performed, and the algorithm, as described above, continued. However, as the bead was comparable to the size of cells within the zebrafish, downsampling would sometimes cause the algorithm to fail. Each time series was checked visually at the output, where the window (Green square) followed the bead (Circled red) Fig. 1.5a. If a time series was seen to fail (likely to occur at the first frame), the second technique would be employed, whereby a user would manually position the initial window to ensure the fine fast tracking could continue. All trajectories in which cells adjacent to the bead underwent cell division or large autonomous displacements were excluded.



(a) Template matching of an ideal fluorescent bead, with a volume of zebrafish tissue, produces a volume image with a single maximum peak where the bead resides.

(b) Here, the red circle represents a well localised single bead.

Fig. 1.5 Template matching used to localise bead positions through time and in 3D.

Sub-pixel tracking

During template matching, the output of the cross-correlation of a template and an image volume has a maximum value at the position where correlation is the highest. For the described algorithm, the highest peak is the most likely candidate for a bead being matched. As such, the simplest way of tracking a bead in a window is to return the cartesian coordinates of that largest value pixel. However, the pixel values in the immediate vicinity of the highest pixel value steadily ramp up. This phenomenon is overcome by fitting a smooth Gaussian local to the maximal peak, allowing a sub-pixel resolved series of coordinates to be found. A more complicated, but more accurate, technique for sub-pixel tracking is to fit a b-spline to the data. The result of a spline fitting offers a smooth fit to what is assumed to be continuous, smooth data, so that the spline itself interpolates the underlying data. Therefore, large bead positioning accuracy can reach beyond the diffraction limit.

1.3.3 Cell tracking

In addition to studying the movement of the bead, we also investigated the movement of nearby cells, with respect to the bead being moved. To track their movements and deformation, a 3D watershed algorithm was written in IDL and applied to membrane-only imaging data. A two-colour zebrafish imaging technique was considered wherein one channel was fluorescent in the nuclei, whilst another

channel was fluorescent exclusively in the membranes. However, the time resolution would have had to have been halved to allow for this, given the system constraints. Although it was possible to add a dichroic image splitter or an additional camera if necessitated, this approach would have halved the overall image resolution in the y axis, and would have added significant complexity and cost. And so, imaging the membranes exclusively provided sufficient information to elucidate the movement and deformation of cells in close proximity to the bead.

1.4 Results

1.4.1 Micro-rheology reveals an increase in the stiffness and elasticity of cells during high- to sphere- stage transition

Even though it has been speculated that morphogenetic change must depend upon changes in the physical properties of tissues, there is little direct evidence to support this idea. This study intended to verify whether the changes that are observed in cell movements and protrusive activity during the high- to sphere-stage transition were accompanied by a modulation of physical properties of the blastoderm. To address this question, magnetic tweezers were used to apply a direct a known force to a $40\text{ }\mu\text{m}$ diameter superparamagnetic bead implanted into the blastoderm [1]. Beads were implanted in blastula-stage embryos and the cells surrounding them were imaged for up to 8 hours. No changes were detected in local cell arrangement, actin-cytoskeleton organisation or myosin localisation around the beads. Embryos containing a bead developed unperturbed by its presence.

Beads were implanted in blastula-stage embryos and the cells surrounding them were imaged for up to 8 hours. No changes in local cell arrangement, actin cytoskeleton organisation or myosin localisation around the beads were detected. Embryos containing a bead developed unperturbed by its presence. The physical properties of the tissue were measured by applying a calibrated, constant force (in the order of 8 mN) for 1 min and tracking the displacement of the bead during, and after, force application. Force was directed alternately radially towards or away from the yolk at 3 min intervals. Bead trajectories revealed that embryonic tissue acts as a viscoelastic medium. Trajectories invariably showed an initial fast displacement followed by a slower, linear displacement, or *creep*, see Fig. 1.6. Upon release, the bead recoiled rapidly towards its original position in a reversal of the initial fast

displacement. Displacement during the slower creep phase was not recovered, see Fig. 1.6. Between high- to sphere-stage there was a significant and systematic reduction in the magnitudes of all phases of movement, but not in the overall shapes of these trajectories, see Fig. 1.6.

To quantify and further characterise these findings, a parameterised mechanical model (Equation (1.6)), that accounts for the shapes of bead trajectories over time, was fit. The most parsimonious model consisted of a dash-pot in series with a parallel spring and dash-pot, see Fig. 1.2. The dash-pots are characterised by viscous coefficients, η_1 and η_2 , and the spring by an elastic modulus, E . Fitted parameters revealed that E increased by 3 fold ($E_{0\text{ min}} = 2.61 \pm 0.57 \text{ Pa}$; $E_{75\text{ min}} = 7.98 \pm 2.50 \text{ Pa}$) and η_1 increased 1.8 fold ($\eta_{1,0\text{ min}} = 156.1 \pm 58.3 \text{ Pa s}$; $\eta_{1,75\text{ min}} = 286.85 \pm 69.34 \text{ Pa s}$) and η_2 2.5 fold ($\eta_{2,0\text{ min}} = 15.82 \pm 3.20 \text{ Pa s}$; $\eta_{2,75\text{ min}} = 40.20 \pm 10.74 \text{ Pa s}$) over a development time of 75 min. No significant differences were found between the two directions of force application ($p_E > 0.05$, $p_{\eta_1} > 0.05$, $p_{\eta_2} > 0.05$). This trend was seen irrespective of the starting developmental age of the embryo, which may suggest work hardening of the zebrafish. A characteristic time constant of the elastic deformation, τ , can be derived from the ratio of η_2 to E . Despite large changes in both η_2 and E , τ remained largely constant over the developmental time (mean = 5.33 s). This suggests that this tissue may contain a mechanism of self-regulation of τ , or that both E and η_2 are determined by a common feature.

The proposed mechanical models provide a good explanation for the trajectory of the bead during the active force application and the initial recoil period. However, bead movements in the later recovery period were more erratic and were not accounted for by the model. Potentially, these deviations may have resulted from additional processes, such as active cell movements. The fitted mechanical model implies that the tissue can be described by two mechanical elements, namely, a soft viscoelastic component and a purely viscous component. A simple hypothesis would be that the viscoelastic component derives from the mechanics of individual cells, whereas the viscosity component is a measure of cell-cell interaction. This was addressed in two ways. Firstly, changes in cell shapes and rearrangements within the tissue, both during and after bead movement, were visualised and measured; secondly, these measurements were repeated in embryos in which there had been a manipulation of cell adhesion, cell protrusive activity and cell contractility, thereby testing the roles of these parameters in determining mechanical properties.

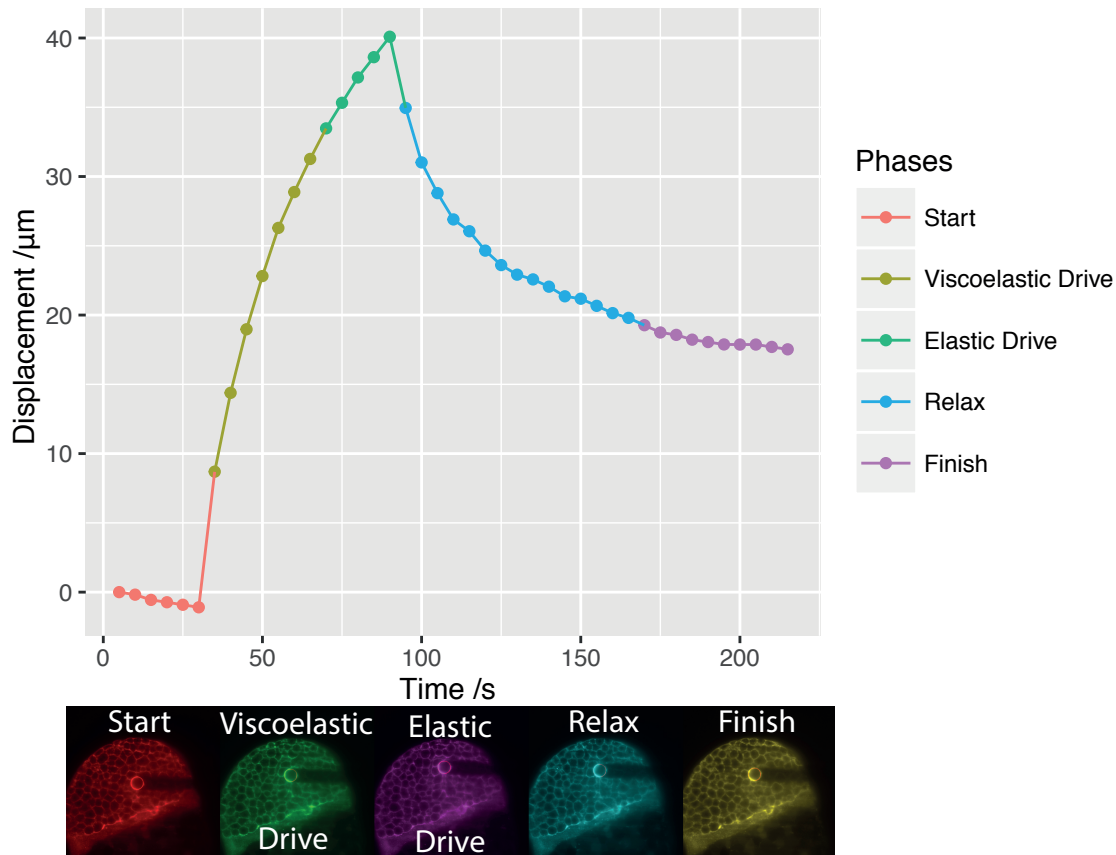
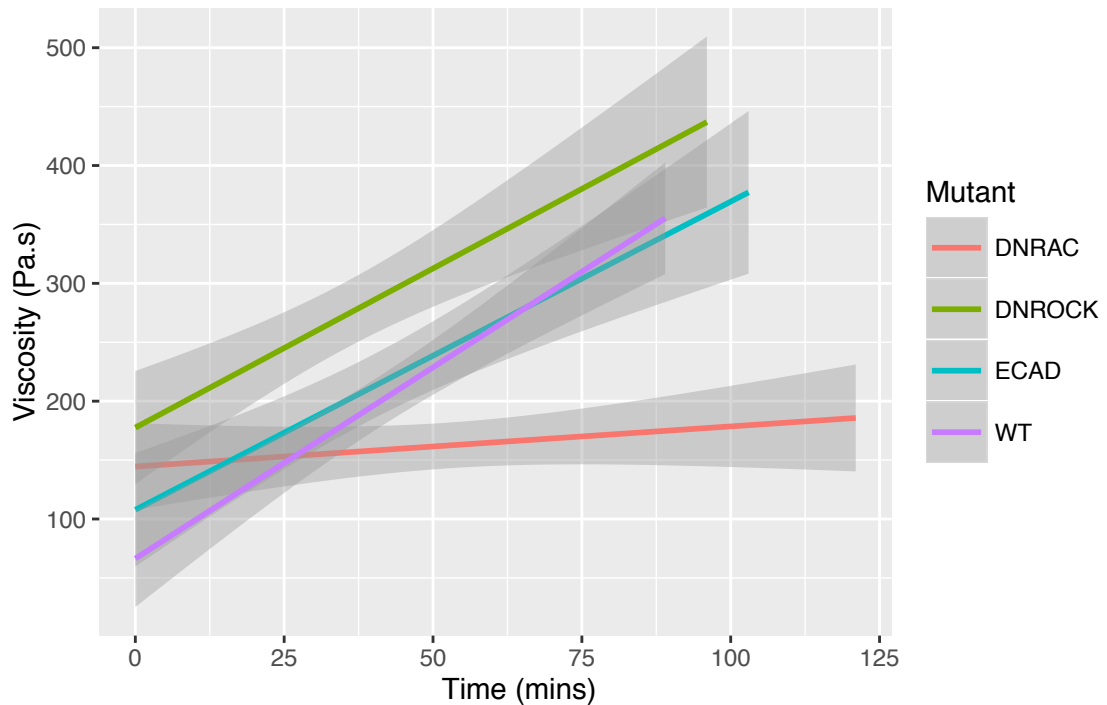
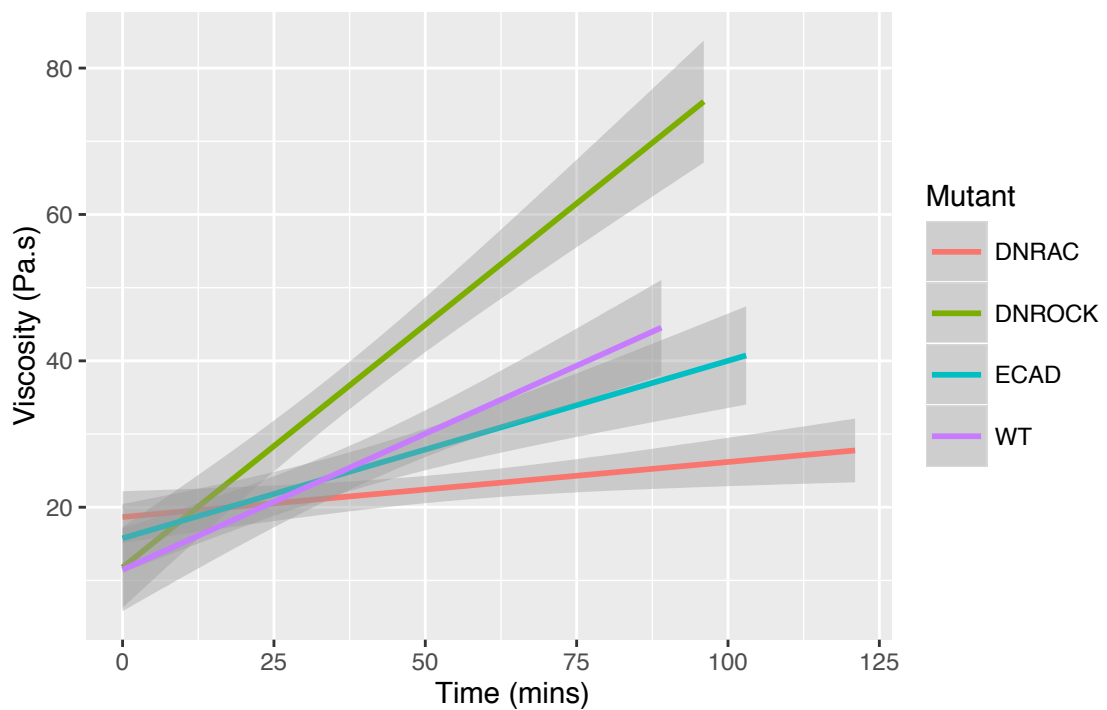


Fig. 1.6 Superraramagnetic bead movement within zebrafish embryonic tissue by a known force shows a trajectory characteristic of viscoelastic behaviour, with a rapid elastic response (*elastic phase*, comprised of the viscoelastic drive), followed by a linear creep period (*creep phase*, comprised of the elastic drive). When the force is removed, the bead is recoiled (*recoil phase*, comprised of a relaxation period and the end of the bead movement).

(a) Change of cellular viscosity η_1 , over time(b) Change of tissue viscosity η_2 over time

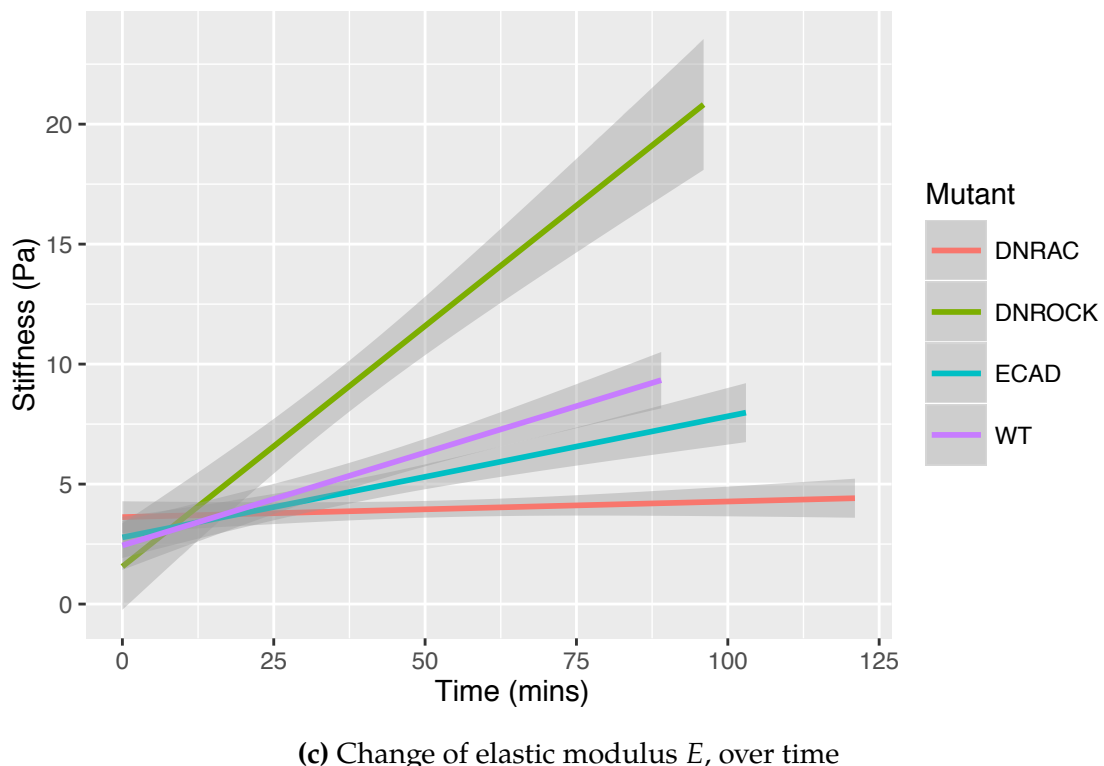
(c) Change of elastic modulus E , over time

Fig. 1.7 Genetic knockdowns have consequences on the developmental evolution of rheological parameters in zebrafish, viscosity coefficients, η_1 (a1.7a) and η_2 (a), and elastic modulus, E (1.7c), are decreased in MoECad ($n=151$ pulls, 9 embryos), and dominant-negative Rac1 gene construct (DNRAC) ($n=158$ pulls, 9 embryos) genotypes, while they are increased in the dominant-negative Rho-kinase construct (DNROCK) ($n=107$ pulls, 9 embryos) genotype compared to WT ($n=178$ pulls, 9 embryos). Not experiments are shown to terminate together as some specimens did not survive the full 2 h course of the experiment.

1.4.2 Elasticity is linked with cell shape deformation and viscosity with cell rearrangement

To examine how cells around the bead responded during the force application fast volumetric light-sheet imaging combined with magnetic tweezers enabled the simultaneous tracking of cell shapes and positions during mechanical probing (Figure 1.8 (a)-(b)). The time course was partitioned into five epochs, based upon the experimental protocol, and the mechanical signatures as described above. The elastic phase was defined as $3 \times \tau$ (spanning 95 % of the elastic duration). The remaining period of active bead displacement was defined as the creep phase. Finally, a 3τ period of elastic recoil was analysed as the recoil period. Cell outlines and positions were automatically tracked, manually omitted and corrected. Cell shape changes and cell displacements were measured along the axis of force application to the bead.

Four sectors were defined around the bead relative to this axis (Fig. 1.8 (a)); here, only the front and rear sectors were considered. In front of the bead, during the elastic period, cells were both compressed and displaced forward by its movement (Fig. 1.8 (c), (d)). This tendency of cells to deform diminished over development time (Fig. 1.8 (f), $p_{\text{linear-regression}} = 0.016$). In fact, cell shape strain rates were highly correlated with, and largely account for, tissue deformation strain rate (Fig. 1.8 (f), $p_{\text{correlation}} = 0.0001757$, $R^2 = 0.743$). The cell shape strain rate coefficient correlated with E (Fig. 1.8 (i), $p_{\text{correlation}} = 0.0449$, $R^2 = 0.453$). Behind the bead, we observed a complementary pattern of cell and tissue stretching ($p_{\text{correlation}} = 0.0748$, $R^2 = 0.473$) at all except the earliest developmental stages. Incomplete cell adhesions, which in turn created holes in the tissue when the bead moved with excess force, may be the cause of this effect. For these cases, cell shape change strain rates did not correlate with tissue deformation strain rate. When the magnetic force was no longer applied, previously compressed cells ahead of the bead re-expanded back along the force axis (Fig. 1.8 (d), (h) $p_{\text{linear-regression}} = 0.016$). Previously stretched cells behind the bead then contracted as the bead recoiled backwards (Fig. 1.8 (d)). There was a strong correlation between E and the rate of expansive cell shape deformation in front of the bead (Fig. 1.8 (k), $p_{\text{correlation}} = 0.016$, $R^2 = 0.53$). This is consistent with the rapid elastic bead recoil being determined by an elastic recoil in cell shape, after the release of the imposed force. In conclusion, the cellular signature of the elastic periods were largely accounted for by cell shape deformations.

¹Figure currently being prepared for publication, reproduced with permission from Dr. Julien Dumortier

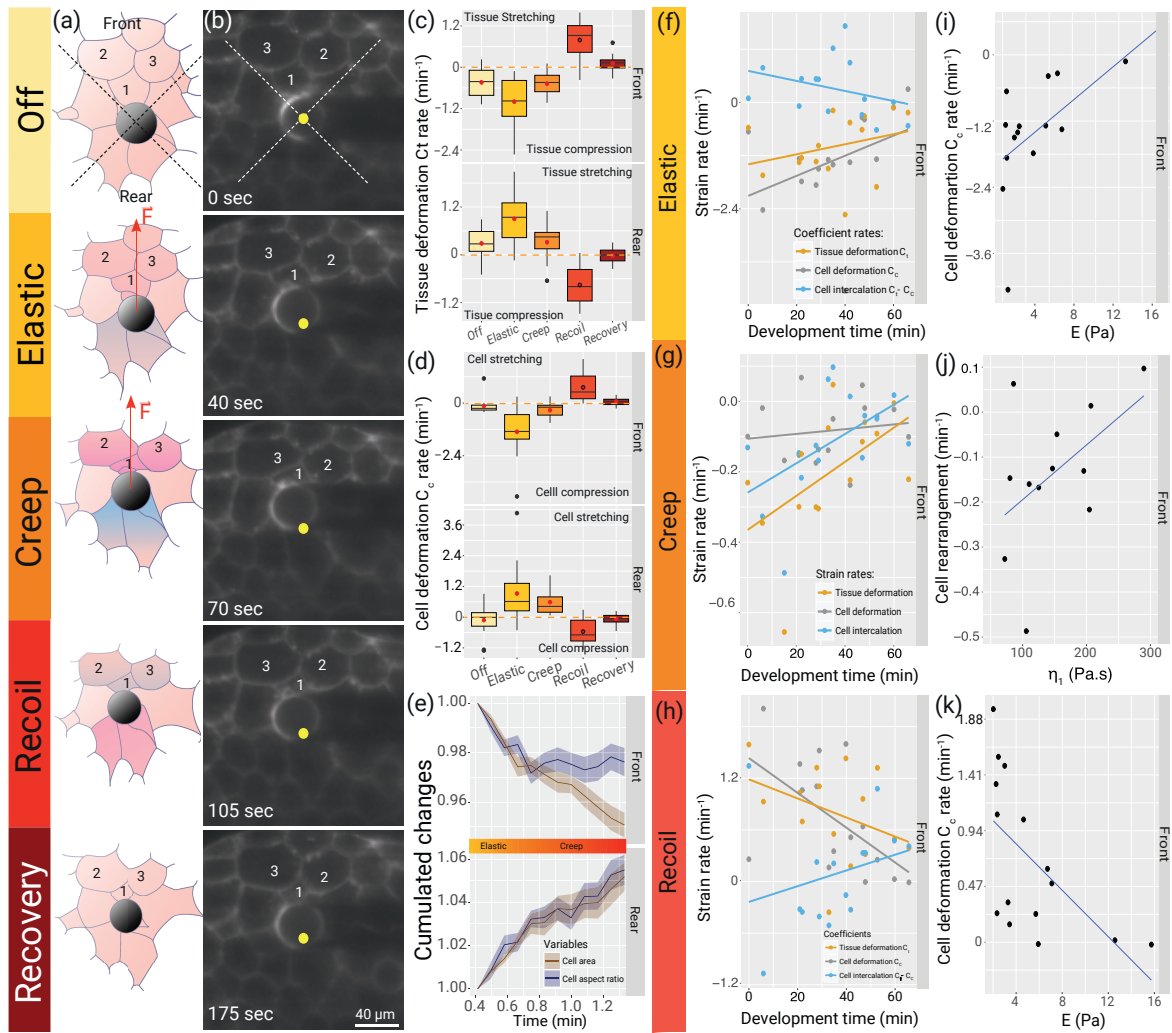


Fig. 1.8 Sketch of the dynamics in a typical rheological experiment (a) in WT embryo under LSFM (b), where blue represents cell extension and red represents compression. The labels 1, 2 and 3 follow respective cells over time. The yellow dot in the LSFM images marks the original position of the bead centre. (c)-(d): Analysis of the coefficient of deformations C_t and C_c showed that tissue (c) and cells (d) were compressed at the front of the bead while they were stretched at the rear during bead pulling ($n = 14$ pulls, 3 embryos). (e)-(h): Analysis of cell area and cell aspect ratio revealed that cells disappear from the imaging plane, suggesting that cells at the front rearranged in 3D, while at the rear, cells were stretched (e). Along developmental time, tissue deformation (C_t), cell deformation C_c and cell intercalation ($C_t - C_s$ during elastic phase ($\text{in } \mu\text{m}^2 \text{min}^{-1}$)), at the front of the bead, show that tissue compression could be accounted for mainly by cell shape changes (f), while, during creep phase, strain rates showed that this accountancy is lost, suggesting cell rearrangement is a major event (g). When force was released, cells at the front relaxed to their original shape (h). (i)-(k): Correlation analysis of cell parameters and rheological parameters. This is supported by correlations between elastic modulus, E , and cell shape change coefficient during elastic phase, at the front of the bead (i), between viscosity coefficient, η_1 , and cell rearrangement rate during creep phase (j), and between elastic modulus, E , and cell shape change coefficient during recoil phase (k). Lines represent linear regressions.

To investigate how tissue deforms during the creep phase, which is defined by η_1 in the mechanical model, the behaviour of cells in the tissue at the front and rear of the bead were visually inspected. Cells became more compressed and moved out of the imaging plane (decreasing in area) in front of the bead and, conversely, cells became stretched and entered the plane at the rear (Fig. 1.8 (a), (b)). This behaviour may be quantified by comparing changes in cell aspect ratio and area through both the elastic and creep periods (Fig. 1.8 (e)). Early cell shape changes gave way to area changes during the creep period; this may be interpreted as the result of cells rearranging in the tissue in front of and behind the bead.

While the elastic periods were dominated by changes in cell shape, the creep period was characterised by cell rearrangements. Cell shape strain accounted for a small fraction of tissue strain rate (Fig. 1.8 (g)), and did not correlate with η_1 ($R^2_{\text{front}} = 0.345, p = 0.21; R^2 = 0.052, p = 0.85$). Nonetheless, measurable cell shape strain rates indicated that some contribution persisted through the creep period. However, cell intercalation strain rate correlated with η_1 , both in front of (Fig. 1.8 (j)) ($p_{\text{correlation}} = 0.0638, R^2 = 0.49$) and behind the bead ($p = 0.035, R^2 = 0.546$). Cell rearrangements appeared to be the major determinants of tissue viscosity in the creep period.

1.4.3 Modifications of cell motility and migration lead to defects in early embryogenesis and tissue rheology

The results of analysing movement during bead displacement were consistent with our simple hypothesis of a two-component model in which the viscoelastic component of tissue perturbation is derived from the mechanics of individual cells, while the component designating only viscosity is a measure of cell-cell interaction. To study how changes in these parameters affect embryo development, and the mechanical properties of the blastoderm, we employed a genetically altered line of zebrafish deficient in E-Cadherin (CDH1) expression. E-Cadherin is an essential transmembrane protein which mediates cellular adhesion, a fundamental requirement for building a cohesive tissue. To achieve this, we employed a knockdown Morpholino approach (MoECad) [ref] for cell adhesion, which lead to defects in the high-to-sphere transformation; these embryos failed to achieve a spherical shape (Figure 5.8 A). Rheological measurements showed that MoECad-treated embryos remained less stiff and less viscous than their wildtype counterparts. Furthermore,

they were reduced in their ability to elevate these properties over developmental time (Figure 5.7), resulting in developmental trends that were significantly different to the WT genotype. Cell migration and cell protrusive activity are two important cell behaviours in the blastoderm. Small enzymes able to hydrolyse the nucleotide guanosine triphosphate (termed GTPase enzymes) have been identified as central orchestrators of cell polarity and motility [ref]. Thus, we manipulated two complementary GTPase components of cell protrusion and migration. The signalling of the GTPase Ras-related C3 botulinum toxin substrate 1 (Rac1) was inactivated by using a DNRAC, []. The same approach was employed to inactivate the signalling of the GTPase Ras homolog gene family, member A (RhoA) by introducing a DNROCK []. DNRAC has been shown to eliminate protrusive activity mediated by Rac1 [], while DNROCK has been shown to reduce the activation of the molecular motor, myosin II, which mediates cellular migration [references]. The injection of these dominant negative constructs affected early morphogenesis; DNRAC-injected embryos failed to progress to a spherical shape, while DNROCK injection caused an accelerated high-to-sphere transition. As expected, our measurement of these rheological parameters by magnetic bead displacement confirmed these predictions: DNRAC embryos failed to increase in stiffness and viscosities η_1 and η_2 ($p_E = 1.016 \times 10^9$, $p_{\eta_1} = 1.876 \times 10^4$, $p_{\eta_2} = 0.0028$), while DNROCK embryos became stiffer and more viscous ($p_E = 7.59e - 25$, $p_{\eta_1} = 6.74 \times 10^{-15}$, $p_{\eta_2} = 3.65 \times 10^{-12}$) than their WT counterparts (Fig. 1.8 (f)-(h)) τ was affected by these knockdowns, as stiffer embryo showed a shorter τ than softer ones ($p \ll 1e - 5$).

1.4.4 Changes in rheological properties for DNRAC and DNROCK treatments are reflected in the rates of cell and tissue deformation

Fast light-sheet imaging analyses were repeated with each knockdown treatment to follow cell behaviours during force application. The resultant parameters segregated according to their mechanical properties: softer DNRAC embryos presented more cell deformation during the elastic period ($p_{WT-DNRAC} = 0.0013$) and more cell rearrangement during the creep period ($p_{WT-DNRAC} = 0.0025$), compared to WT. Cells in the stiffer DNROCK-injected embryos deformed less in the elastic period ($p_{WT-DNROCK} = 0.0017$) and exhibited fewer cell rearrangements in the creep period ($p_{WT-DNROCK} = 0.0013$) (1.8 (j)). These results confirm that the

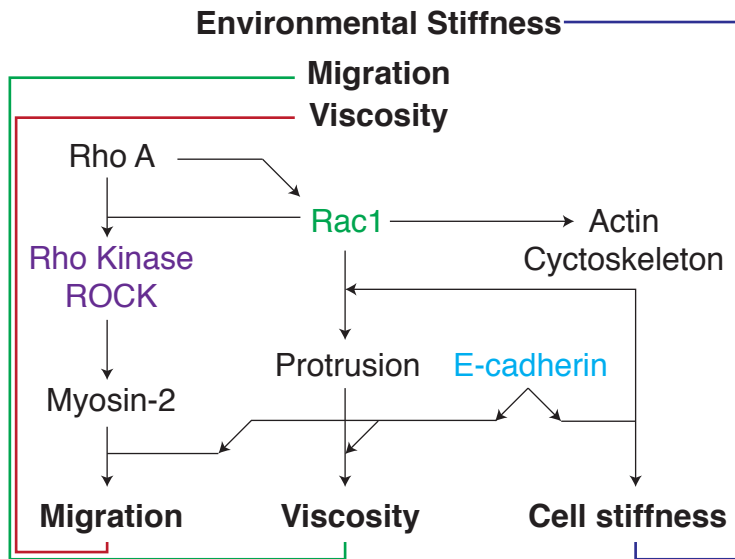


Fig. 1.9 Summary of effects of knockdowns in cell motion, cell protrusive activity and cell adhesion through the loss of function of Rac1, DNROCK and E-Cadherin. Based on literature, a feedback mechanism via mechano-sensing through Rac1 (blue, red and green arrows) is speculated to regulate the tissue rheology. Rac1 activation promotes actin cytoskeleton elaboration, increasing cell stiffness, and the production of cell protrusions. Protrusions provide a means of elaborating cell-cell adhesion, increasing tissue viscosity and enabling motility. Motility is achieved by contraction relative to points of adhesion, providing both movement and effectively testing the mechanical compliance of the cell network, feeding back to activate Rac1.

previously-observed correlations between cellular and rheological parameters hold true under this expanded range; stiffness, E , is strongly correlated with initial cell shape deformation, while η_1 is strongly correlated with cell rearrangements. This suggests that there may be a relatively simple cellular interpretation of the physical model measured using magnetic bead rheology.

1.5 Discussion

The study presented here is the first demonstration of a direct link between cell behaviours and embryo morphogenesis arising from changing mechanical properties. By applying a directed local force to a developing embryo, through an embedded magnetic bead, local and ensemble mechanical properties of tissue were characterised. The blastula tissue was shown to have an intrinsic viscoelastic response; the data showed that tissues exhibit fluid-like behaviours, as observed in previous studies

using optical tweezers in mature epithelia, [] and magnetic droplets injected into much older fish than considered here []. The viscoelastic timescale parameter, τ , remained constant across both time and embryonic mutations. The results of this study elucidate the biological meaning of the rheological parameters of viscosity and elasticity in terms of cellular morphology changes and rearrangement.

The viscous and elastic components are involved in cell shape, intercalation and deformation. Increased stiffness is related to less deformable cells, and increased viscosity to diffusivity of cells during rearrangement. In developing wildtype embryos, prior to bulging, the blastula becomes 3-fold more viscous and stiff. Tissue viscosity, in the form of cell rearrangement, is a measure of the friction imposed by cell-cell connections, which may be mediated by cell protrusions and E-cadherin adhesion. Rac1 activity would then follow to promote viscosity and cell stiffness by increasing the polymerisation of actin and encouraging cell-cell adhesions via E-cadherin connections. Yet, the decrease in cell stiffness with MoECad treatment suggests a more complicated coupling. We propose that a cellular mechanotransduction mechanism assays the compliance of the environment between sites of adhesion. It is well understood that cells grown on a surface adjust their mechanical stiffness in proportion to substrate stiffness. In the case of early mesenchymal tissues, we suggest that the cells themselves collectively constitute their own local mechanical environment, coupled via protrusion-promoted cell-cell adhesion. Numerous examples exist of mesenchymal cells interacting via protrusions []. During collective migration, cadherin-mediated cell-cell connections are able to promote cell polarisation and cytoskeletal rearrangements, acting through Rac1 activation []. Given the role of protrusions in both motility and transduction, this relationship explains the close correlation between viscosity and stiffness.

The emergence of cohesive mesenchymal tissue mechanical properties may be linked with the motility of its cells and, in particular, the formation of protrusions that facilitate the establishment of cadherin-based cell-cell adhesions. Connectivity could result in an actin superstructure networked between cells, through cell adhesion proteins. Tissue stiffness and viscosity are well-correlated with the number of protrusions present and it is possible that these mechanisms might be found in other mesenchymal tissues during development []. These findings highlight a potentially fundamental difference in the determination of mechanical properties between epithelial and mesenchymal tissues. Epithelial cells represent relatively static configurations, based upon adhesion and contraction, while mesenchymal

cells are adhesive and stiff, but dependent upon dynamic protrusion-based motility. The stiffening blastula, composed of radially anisotropic cells, is thus poised to drive blastula thinning and yolk bulging in the next morphogenetic movement of the zebrafish embryo.

References

1. Gilbert, S. F. *Developmental Biology* 6th (Sinauer Associates, 2000).
2. Wolpert, L. *Principles of Development* (Oxford University Press, USA, 2006).
3. *Animal Models of Human Disease: Zebrafish Swim into View.* - PubMed - NCBI
<https://www.ncbi.nlm.nih.gov/pubmed/17440532> (2018).
4. L.D. Landau & E.M. Lifshitz. *Theory of Elasticity* ().
5. Wilcox, R. R. The Percentage Bend Correlation Coefficient. *Psychometrika* **59**, 601–616 (1994).